

# Hallucinating Bag-of-Words and Fisher Vector IDT terms for CNN-based Action Recognition

Lei Wang<sup>\*,1,2</sup> Piotr Koniusz<sup>\*,1,2</sup> Du Q. Huynh<sup>3</sup>

<sup>1</sup>Data61/CSIRO, <sup>2</sup>Australian National University, <sup>3</sup>University of Western Australia  
firstname.lastname@{data61.csiro.au<sup>1</sup>, anu.edu.au<sup>2</sup>, uwa.edu.au<sup>3</sup>}

## Abstract

*In this paper, we revive the use of old-fashioned hand-crafted video representations and put new life into these techniques via a CNN-based hallucination step. Specifically, we address the problem of action classification in videos via an I3D network pre-trained on the large scale Kinetics-400 dataset. Despite of the use of RGB and optical flow frames, the I3D model (amongst others) thrives on combining its output with the Improved Dense Trajectory (IDT) and extracted with it low-level video descriptors encoded via Bag-of-Words (BoW) and Fisher Vectors (FV). Such a fusion of CNNs and hand crafted representations is time-consuming due to various pre-processing steps, descriptor extraction, encoding and fine-tuning of the model. In this paper, we propose an end-to-end trainable network with streams which learn the IDT-based BoW/FV representations at the training stage and are simple to integrate with the I3D model. Specifically, each stream takes I3D feature maps ahead of the last 1D conv. layer and learns to ‘translate’ these maps to BoW/FV representations. Thus, our enhanced I3D model can hallucinate and use such synthesized BoW/FV representations at the testing stage. We demonstrate simplicity/usefulness of our model on three publicly available datasets and we show state-of-the-art results.*

## 1. Introduction

Action Recognition pipelines, or AR for short, have undergone over the decade a transition from hand-crafted video descriptors [12, 50, 29, 58, 59, 60] to CNN-based pipelines [51, 54, 15, 4]. Examples of new powerful CNN architectures include the two-stream network [51], 3D spatio-temporal features [54], spatio-temporal ResNet model [15] and the new I3D network pre-trained on Kinetics-400 [4]. However, these powerful networks op-

\*Both authors contributed equally. Please respect the authors’ efforts by not copying/plagiarizing bits and pieces of this work for your own gain (we will vigorously pursue dishonest authors). If you find anything inspiring in this work, be kind enough to cite it thus showing you care for the CV community. An update with results on the Charades dataset will follow shortly.

erate on the RGB and optical flow frames thus failing to capture some domain-specific information which sophisticated low-level representations capture by design. One prominent example are Improved Dense Trajectory (IDT) descriptors [60] which are typically encoded with Bag-of-Words (BoW) [52, 11] or Fisher Vectors (FV) [43, 44] and fused with the majority of the modern CNN-based approaches [19, 7, 8, 61, 9] at the classifier level for the best performance. To understand why CNN-based action recognition pipelines improve their performance upon a fusion with the IDT representations, one has to note that IDT involve several sophisticated steps: (i) camera motion estimation, (ii) modeling motion descriptors along motion trajectories captured with the optical flow, (iii) pruning inconsistent matches, (iv) removing focus from humans by the use of a human detector, *etc.* Moreover, dense trajectories are typically combined with powerful video descriptors such as Histogram of Oriented Gradients (HOG) [20, 29], Histogram of Optical Flow (HOF) [12] and Motion Boundary Histogram (MBH) [59], or even SIFT3D [50] which are highly complementary to each other *e.g.*, HOF and MBH contain zero- and first-order motion statistics [60].

However, extracting dense trajectories and corresponding video descriptors is a costly task, often performed off-line off-GPU, due to time-consuming steps described above. Motivated by such a shortcoming, we propose simple trainable CNN streams on top of a CNN network (in our case I3D [4]) which are able to learn and ‘translate’ the I3D output into IDT-based BoW and FV global video descriptors. At the testing stage, our so-called BoW and FV streams are able to hallucinate these global descriptors from the I3D outputs. Thus, we feed them into the remaining part of the pipeline combined with a classifier. Our simple approach demonstrates that sophisticated handcrafted representations can be synthesized by the network thus removing the need of actual computations of IDT representations, thus simplifying the overall action recognition pipeline. Depending on an employed variant of our streams, with a handful of convolutional layers or FC layers, and other basic CNN building blocks, we achieve a representation which rivals sophisticated action recognition pipelines that realize complex strategies for aggregation of frames *e.g.*, higher-

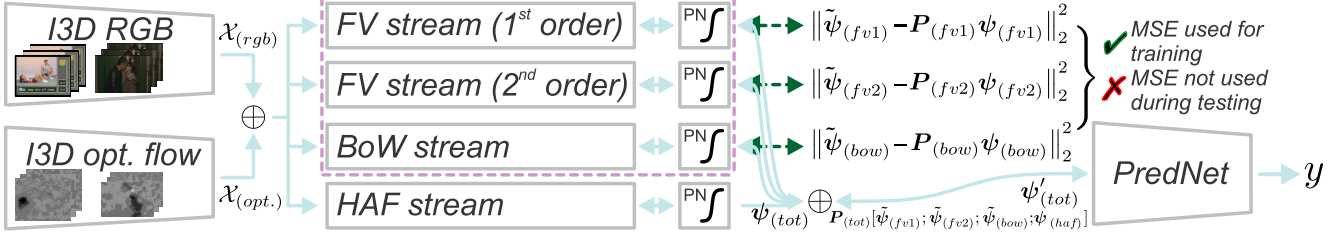


**Figure 1:** The overview of our pipeline. We remove the prediction and the last 1D conv. layers from I3D RGB and optical flow streams, concatenate ( $\oplus$ ) the  $1024 \times 7$  feature representations  $\mathcal{X}_{(rgb)}$  and  $\mathcal{X}_{(opt.)}$ , and feed them into our *Fisher Vector (FV)*, *Bag-of-Words (BoW)*, and *the High Abstraction Features (HAF)* streams followed by the *Power Normalization (PN)* blocks. The resulting feature vectors  $\tilde{\psi}_{(fv1)}$ ,  $\tilde{\psi}_{(fv2)}$ ,  $\tilde{\psi}_{(bow)}$  and  $\tilde{\psi}_{(haf)}$  are concatenated ( $\oplus$ ) and fed into our *Prediction Network (PredNet)*. By  $\checkmark$ , we indicate that the three Mean Square Error (MSE) losses are only applied at the training stage to train our FV (first- and second-order components) and BoW hallucinating streams (indicated in dashed red). By  $\times$ , we indicate that the MSE losses are switched off at the testing stage. Thus, we hallucinate  $\tilde{\psi}_{(fv1)}$ ,  $\tilde{\psi}_{(fv2)}$  and  $\tilde{\psi}_{(bow)}$ , and pass them to PredNet together with  $\psi_{(haf)}$  to obtain labels  $y$ . The original training FV and BoW feature vectors (used only during training) are denoted by  $\psi_{(fv1)}$ ,  $\psi_{(fv2)}$  and  $\psi_{(bow)}$  while  $\mathbf{P}$  are count sketch projecting matrices (see text for details).

order pooling [7] and rank-pooling [19, 8, 61, 9]. Below, we detail our contributions:

- I. We are the first to propose that old-fashioned IDT-based BoW and FV global video descriptors can be learned via simple dedicated CNN-streams at the training stage and simply hallucinated for classification with a CNN action recognition pipeline during testing.
- II. We investigate various aspects of our network by incorporating so-called count sketching [45] of features to prevent overfitting when fusing several streams, Power Normalization [35, 34, 36] to prevent so-called burstiness in BoW, FV and CNNs, and we include an ablation study by removing various blocks of our network.
- III. We perform several experiments on three standard publicly available video recognition benchmarks thus demonstrating the usefulness of our idea.

The reminder of this paper is organized as follows. Section 2 discusses background works and their relation to our approach. Section 3 introduces notations and necessary concepts. Section 4 outlines our approach. Finally, Sections 5 and 6 present our empirical results and conclusions.

## 2. Related Work

In what follows, we describe related works such as early hand-crafted spatio-temporal representations of videos and their encoding strategies, optical flow representations, and deep learning pipelines dedicated to video classification followed by related aggregation strategies.

**Handcrafted video representations.** Early action recognition approaches relied on various spatio-temporal interest point detectors [39, 13, 5, 65, 40, 58] and spatio-temporal descriptors [12, 50, 55, 58, 59, 60] which were designed to capture various appearance and motion statistics.

Spatio-temporal interest point detectors were developed for the task of identifying spatio-temporal regions of videos

rich in motion patterns relevant to classification. Such resulting interest points then carry sampling information for descriptors and, depending on the number of key-points, they influence the processing speed which is of concern due to the volumetric nature of videos. Harris3D [39], one of the earliest detectors, performs a search for extreme points in the spatio-temporal domain by the use of the so-called structure tensor and the determinant-to-trace ratio test. Cuboid [13], a much faster alternative detector, separately applies Gaussian and Gabor filters in spatial and temporal domains. Selective STIP [5] extracts initial key-point candidates with the Harris corner detector followed by the candidate suppression with a so-called surround suppression mask. Hes-STIP, a more recent detector, uses integral videos and Hessian matrix to search the scale-space for local maxima of the signal. Evaluations and further reading on spatio-temporal detectors can be found in a survey [21].

One drawback of spatio-temporal interest point detectors is the sparsity of key-points and inability to capture long-term motion patterns. Thus, a Dense Trajectory (DT) [58] approach densely samples feature points in each frame to track them in the video by the use of optical flow. Then, multiple descriptors are extracted along trajectories to capture shape, appearance and motion cues. As DT descriptors cannot compensate for the camera motion, an Improved Dense Trajectory (IDT) [60, 59] uses estimates of camera motion to remove the global background motion. Additionally, to minimize the focus on humans performing actions, IDT removes inconsistent matches via a human detector.

For spatio-temporal descriptors, IDT employs Histogram of Oriented Gradients (HOG) [20], Histogram of Optical Flow (HOF) [12] and Motion Boundary Histogram (MBH) [59]. HOG [20] contains statistics of the amplitude of image gradients w.r.t. the gradient orientation. Thus, it captures the static appearance cues while its close cousin, HOG-3D [29], is designed for spatio-temporal interest points. HOF [12] is a descriptor which captures his-

tograms of optical flow. MBH [59] captures derivatives of the optical flow, thus it is highly resilient to the global camera motion whose cues cancel out due to derivatives. Thus, HOF and MBH contain the zero- and first-order optical flow statistics. Other spatio-temporal descriptors include SIFT3D [50], SURF3D [65] and Local Trinary Patterns [66], a cousin of well-known LBPs.

In this work, we use the Improved Dense Trajectories with HOG, HOF, and MBH. Following the standard steps in action recognition [58, 7, 9], we encode trajectories together with these descriptors via Bag-of-Words (BoW) [52, 11] and Fisher Vectors (FV) [43, 44] which we describe below.

**Descriptor encoding.** Bag-of-Words [52, 11], a global image representation inspired by natural language processing, is one of the oldest and simplest local descriptor encoding strategies. In its simplest form, it consists of (i) clustering with k-means a collection of descriptor vectors from the training set to build so-called visual vocabulary, (ii) assigning each descriptor to its nearest cluster center from the visual dictionary, and (iii) aggregating the one-hot assignment vectors via average pooling. Further improvements, so-called Soft Assignment (SA) [56, 31] and Localized Soft Assignment (LcSA) [41, 35], use the Component Membership Probability (CMP) of GMM to assign each descriptor with some probability to each/k-closest visual words followed by average pooling or other aggregators [35].

In this paper, for simplicity, we chose the simplest BoW, as in [11], followed by so-called Power Normalization [35] which we will describe in Section 3. As BoW can be seen as zero-order statistics of Fisher Vectors [43, 44], we also employ FV to capture first- and second-order statistics of local descriptors. FV builds a visual dictionary from training datapoints via GMM. Then, a displacement/square displacement of each descriptor vector w.r.t. each GMM component center is taken, normalized by its GMM standard deviation/variance to capture the first/second-order statistics, and then soft-assigned via CMP to each GMM component.

**Optical flow.** Optical flow, a key concept in action recognition from videos, is defined as the pattern of motion of objects, surfaces and edges in a visual scene caused by the relative motion between an observer and a scene [25]. It is the distribution of velocities of movement of brightness pattern across frames [24]. Early optical flow coped with small displacements via energy minimization [24] and, by surface warping, it could yield very accurate estimations [42]. However, to capture informative motions of subjects and objects in videos, optical flow needs to cope with large displacements [1]. As energy-based methods suffer from the local minima, local descriptor matching is used in Large Displacement Optical Flow (LDOF) [3]. Recent methods use non-rigid descriptor matching [64], segment matching [2] or even edge-preserving interpolation on a sparse set of matches to deal with occlusions [47].

In this work, we are not concerned with the use of the newest possible optical flow. Thus, we opt for LDOF [42].

**CNN-based action recognition.** The success of AlexNet [37] and ImageNet [49] sparked studies into action recognition with CNNs. Early CNNs extracted per-frame representations followed by average pooling defined as an average over feature vectors [28] which discards the information about the temporal order. To alleviate such a shortcoming, frame-wise CNN scores can be combined with LSTMs [14]. Two-stream networks [51] compute representations per RGB frame and per 10 stacked optical flow frames. However, a more obvious extension is to model spatio-temporal 3D CNN filters [27, 54, 15, 57].

The above pipelines have various merits and drawbacks, thus the I3D model [4] draws on the two-stream networks, ‘inflates’ 2D CNN filters pretrained on ImageNet to spatio-temporal 3D filters, and implements temporal pooling across the inception module. In this paper, we opt for the I3D network but our proposed layers are independent of the CNN design. Instead, we are concerned with ‘absorbing’ the old yet powerful IDT representations into the CNN pipeline and hallucinating them at the test time.

**Temporal aggregation methods.** While two-stream networks [51] discard the temporal order and other methods use LSTMs [14], there exist many AR pipelines studying spatio-temporal aggregation. Rank pooling [18, 19] performs a linear projection of frame-wise feature vectors onto a line so that the temporal order of vectors is preserved on the line. Further extensions include subspace and kernel rank pooling [8, 61] for which frame-wise subspace representations are projected in the RKHS for the temporal order to be preserved. Another family of pooling methods capture second- or higher-order statistics [7, 30, 34].

In this paper, we are not concerned with the temporal pooling step. Thus, we use a 1D convolution (as in I3D [4]) to factor out the temporal dimension of feature maps.

**Power Normalization family.** Bag-of-Words, Fisher Vectors and even CNN-based descriptors have to deal with the so-called burstiness defined as ‘*the property that a given visual element appears more times in an image than a statistically independent model would predict*’ [26], a phenomenon also present in video descriptors. Power Normalization [35, 33] is known to suppress the burstiness, and it has been extensively studied and evaluated in the context of Bag-of-Words [35, 33, 34, 36]. Moreover, a connection to Max-pooling was found in survey [35] which further shows that so-called MaxExp feature pooling is in fact a detector of ‘*at least one particular visual word being present in an image*’. According to papers [35, 36], many Power Normalization functions are closely related. We outline Power Normalizing functions used in our work in Section 3. Below, we describe the mathematical prerequisites on which we build.

**Why does it work?** IDT perform camera motion estimation and capture motion information along motion trajectories (tracked along sequence) while pruning inconsistent matches. Such operations are unlikely to be captured by off-the-shelf CNNs unless a CNN is enforced by some constraints to learn IDT. We perform translation of the I3D output into IDT-based BoW and FV global video descriptors by applying the MSE loss. Thus, we force I3D network to implicitly learn sophisticated IDT descriptor trajectory modeling. One can think we co-regularize I3D network by forcing it to mimic complementary I3D representation. Our approach is somewhat related to domain adaptation papers where a source domain network co-regularizes a target network [32, 53, 23, 22] by the alignment of feature statistic in both streams. However, we create a dedicated layer which hallucinates BoW/FV representations via an additional layer on top of I3D stream to use them at the test time thus further boosting results. See Appendix A for the quality of the MSE loss.

### 3. Background

In our work, we use BoW/FV (training stage), as well as Power Normalization [35, 34] and count sketches [63].

**Notations.** We use boldface uppercase letters to express matrices *e.g.*,  $\mathbf{M}, \mathbf{P}$ , regular uppercase letters with a subscript to express matrix elements *e.g.*,  $P_{ij}$  is the  $(i, j)^{\text{th}}$  element of  $\mathbf{P}$ , boldface lowercase letters to express vectors, *e.g.*  $\mathbf{x}, \boldsymbol{\phi}, \boldsymbol{\psi}$ , and regular lowercase letters to denote scalars. Vectors can be numbered *e.g.*,  $\mathbf{m}_1, \dots, \mathbf{m}_K$  or  $\mathbf{x}_n$ , *etc.*, while regular lowercase letters with a subscript express an element of vector *e.g.*,  $m_i$  is the  $i^{\text{th}}$  element of  $\mathbf{m}$ . Operators ‘;’ and  $\oplus$  concatenate vectors *e.g.*,  $\oplus_{i \in \mathcal{I}_K} \mathbf{v}_i = [\mathbf{v}_1; \dots; \mathbf{v}_K]$  while  $\mathcal{I}_d$  denotes an index set of integers  $\{1, \dots, d\}$ .

#### 3.1. Descriptor Encoding Schemes

**Bag-of-Words** [52, 11] assigns each local descriptor  $\mathbf{x}$  to the closest visual word from  $\mathbf{M} = [\mathbf{m}_1, \dots, \mathbf{m}_K]$  built via k-means. In order to obtain mid-level feature  $\boldsymbol{\phi}$ , we solve:

$$\begin{aligned} \boldsymbol{\phi} &= \arg \min_{\boldsymbol{\phi}'} \|\mathbf{x} - \mathbf{M} \boldsymbol{\phi}'\|_2^2, \\ \text{s. t. } \boldsymbol{\phi}' &\in \{0, 1\}, \mathbf{1}^T \boldsymbol{\phi}' = 1. \end{aligned} \quad (1)$$

**Fisher Vector Encoding** [43, 44] uses a Mixture of  $K$  Gaussians from a GMM used as a dictionary. It performs descriptor coding w.r.t. to Gaussian components  $G(w_k, \mathbf{m}_k, \boldsymbol{\sigma}_k)$  which are parametrized by mixing probability, mean, and on-diagonal standard deviation. The first- and second-order features  $\boldsymbol{\phi}_k, \boldsymbol{\phi}'_k \in \mathbb{R}^D$  are :

$$\boldsymbol{\phi}_k = (\mathbf{x} - \mathbf{m}_k) / \boldsymbol{\sigma}_k, \quad \boldsymbol{\phi}'_k = \boldsymbol{\phi}_k^2 - 1. \quad (2)$$

Concatenation of per-cluster features  $\boldsymbol{\phi}_k^* \in \mathbb{R}^{2D}$  forms the mid-level feature  $\boldsymbol{\phi} \in \mathbb{R}^{2KD}$ :

$$\boldsymbol{\phi} = [\boldsymbol{\phi}_1^*; \dots; \boldsymbol{\phi}_K^*], \quad \boldsymbol{\phi}_k^* = \frac{p(\mathbf{m}_k | \mathbf{x}, \theta)}{\sqrt{w_k}} \left[ \boldsymbol{\phi}_k; \boldsymbol{\phi}'_k / \sqrt{2} \right], \quad (3)$$

where  $p$  and  $\theta$  are the component membership probabilities and parameters of GMM, respectively. For each descriptor  $\mathbf{x}$  of dimensionality  $D$  (after PCA), its encoding  $\boldsymbol{\phi}$  is of  $2KD$  dim. as  $\boldsymbol{\phi}$  contains first-and second-order statistics.

#### 3.2. Pooling a.k.a. Aggregation

Traditionally, pooling is performed via averaging mid-level feature vectors  $\boldsymbol{\phi}(\mathbf{x})$  corresponding to (local) descriptors  $\mathbf{x} \in \mathcal{X}$  from a video sequence  $\mathcal{X}$ , that is  $\boldsymbol{\psi} = \text{avg}_{\mathbf{x} \in \mathcal{X}} \boldsymbol{\phi}(\mathbf{x})$ , and (optionally) applying the  $\ell_2$ -norm normalization. In this paper, we work with either sequences  $\mathcal{X}$  (for which the above step is used) or subsequences.

**Proposition 1.** *For subsequence pooling, let  $\mathcal{X}_{s,t} = \mathcal{X}_{0,t} \setminus \mathcal{X}_{0,s-1}$ , where  $\mathcal{X}_{s,t}$  denotes a set of descriptors in the sequence  $\mathcal{X}$  counting from frame  $s$  up to frame  $t$ , where  $0 \leq s \leq t \leq \tau$ ,  $\mathcal{X}_{0,-1} \equiv \emptyset$ , and  $\tau$  is the length of  $\mathcal{X}$ . Moreover, let us compute an integral mid-level feature  $\boldsymbol{\phi}'_t = \boldsymbol{\phi}'_{t-1} + \sum_{\mathbf{x} \in \mathcal{X}_{s,t}} \boldsymbol{\phi}(\mathbf{x})$  which aggregates mid-level feature vectors from frame 0 to frame  $t$ , and  $\boldsymbol{\phi}'_{-1}$  is an all-zeros vector. Then, the pooled subsequence is given by:*

$$\boldsymbol{\psi}_{s,t} = (\boldsymbol{\phi}'_t - \boldsymbol{\phi}'_{s-1}) / (\|\boldsymbol{\phi}'_t - \boldsymbol{\phi}'_{s-1}\|_2 + \epsilon), \quad (4)$$

where  $0 \leq s \leq t \leq \tau$  are the starting and ending frames of subsequence  $\mathcal{X}'_{s,t} \subseteq \mathcal{X}$  and  $\epsilon$  is a small constant. We normalize the pooled sequences/subseq. as described next.

#### 3.3. Power Normalization

As alluded to in Section 2, we apply Power Normalizing functions to BoW and FV streams which hallucinate these two modalities (and HAF stream explained later). We investigate three operators  $g(\boldsymbol{\psi}, \cdot)$  described in remarks below.

**Remark 1.** *AsinhE function [36] is an extension of a well-known Power Normalization (Gamma) [36] defined as  $g(\boldsymbol{\psi}, \gamma) = \text{Sgn}(\boldsymbol{\psi}) |\boldsymbol{\psi}|^\gamma$  for  $0 < \gamma \leq 1$  to the operator with a smooth derivative and a parameter  $\gamma'$ . AsinhE is defined as the normalized Arcsin hyperbolic function:*

$$g(\boldsymbol{\psi}, \gamma') = \text{arcsinh}(\gamma' \boldsymbol{\psi}) / \text{arcsinh}(\gamma'). \quad (5)$$

**Remark 2.** *Sigmoid (SigmE), a Max-pooling approximation [36], is an extension of the MaxExp operator defined as  $g(\boldsymbol{\psi}, \eta) = 1 - (1 - \boldsymbol{\psi})^\eta$  for  $\eta > 1$  to the operator with a smooth derivative, a response defined for real-valued  $\boldsymbol{\psi}$  (rather than  $\boldsymbol{\psi} \geq 0$ ), a parameter  $\eta'$  and a small const.  $\epsilon'$ :*

$$g(\boldsymbol{\psi}, \eta') = \frac{2}{1 + e^{-\eta' \boldsymbol{\psi} / (\|\boldsymbol{\psi}\|_2 + \epsilon')}} - 1. \quad (6)$$

**Remark 3.** *AxMin, a piece-wise linear form of SigmE [36], is given as  $g(\boldsymbol{\psi}, \eta'') = \text{Sgn}(\boldsymbol{\psi}) \min(\eta'' \boldsymbol{\psi} / (\|\boldsymbol{\psi}\|_2 + \epsilon'), 1)$  for  $\eta'' > 1$  and a small constant  $\epsilon'$ .*

Despite the similar role of these three pooling operators, we investigate each of them as their interplay with end-to-end learning differs. Specifically,  $\lim_{\psi \rightarrow \pm\infty} g(\psi, \cdot)$  for AsinhE and SigmE are  $\pm\infty$  and  $\pm 1$ , resp., thus their asymptotic behavior differs. Moreover, AxMin is non-smooth and relies on the same gradient re-projection properties as ReLU.

### 3.4. Count Sketches

Sketching vectors by the count sketch [10, 63] is used for their dimensionality reduction which we use in this paper.

**Proposition 2.** *Let  $d$  and  $d'$  denote the input out output dimensionality of the input and sketched output vectors, respectively. Let vector  $\mathbf{h} \in \mathbb{I}_{d'}^d$  contain  $d$  uniformly drawn integer numbers from  $\{1, \dots, d'\}$  and vector  $\mathbf{s} \in \{-1, 1\}^d$  contain  $d$  uniformly drawn values from  $\{-1, 1\}$ . Then, the sketch projection matrix  $\mathbf{P} \in \{-1, 0, 1\}^{d' \times d}$  becomes:*

$$P_{ij} = \begin{cases} s_i & \text{if } h_i = j, \\ 0 & \text{otherwise,} \end{cases} \quad (7)$$

and the sketch projection  $p : \mathbb{R}^d \rightarrow \mathbb{R}^{d'}$  is a linear operation given as  $p(\psi) = \mathbf{P}\psi$  (or  $p(\psi; \mathbf{P}) = \mathbf{P}\psi$  to highlight  $\mathbf{P}$ ).

*Proof.* It directly follows from the definition of the count sketch e.g., see Definition 1 [63].  $\square$

**Remark 4.** *Count sketches are unbiased estimators:  $\mathbb{E}_{\mathbf{h}, \mathbf{s}}(p(\psi, \mathbf{P}(\mathbf{h}, \mathbf{s})), p(\psi', \mathbf{P}(\mathbf{h}, \mathbf{s}))) = \langle \psi, \psi' \rangle$ . As variance  $\mathbb{V}_{\mathbf{h}, \mathbf{s}}(p(\psi), p(\psi')) \leq \frac{1}{d'} (\langle \psi, \psi' \rangle^2 + \|\psi\|_2^2 \|\psi'\|_2^2)$ , we note that larger sketches are less noisy. Thus, for every modality we compress, we use a separate sketch matrix  $\mathbf{P}$ . As video modalities are partially dependent, this implicitly leverages the unbiased estimator and reduces the variance.*

*Proof.* For the first and second property, see Appendix A [63] and Lemma 3 [45].  $\square$

## 4. Approach

Our pipeline is illustrated in Figure 1. It consist of (i) the Fisher Vector and Bag-of-Words hallucinating streams denoted as FV and BoW (shown in dashed red), respectively, (ii) the High Abstraction Features stream denoted as HAF, and (iii) the Prediction Network abbreviated as PredNet.

The role of BoW/FV streams is to take I3D intermediate representations generated from the RGB and optical flow frames and learn to hallucinate BoW/FV representations. For this purpose, we use the MSE loss between the ground-truth BoW/FV and the outputs of BoW/FV streams. The role of the HAF stream is to further process I3D intermediate representations before they are concatenated with hallucinated BoW/FV. The role of PredNet is to simply fuse the concatenated BoW/FV/HAF representations and learn class concepts. Below, we describe each module in detail.

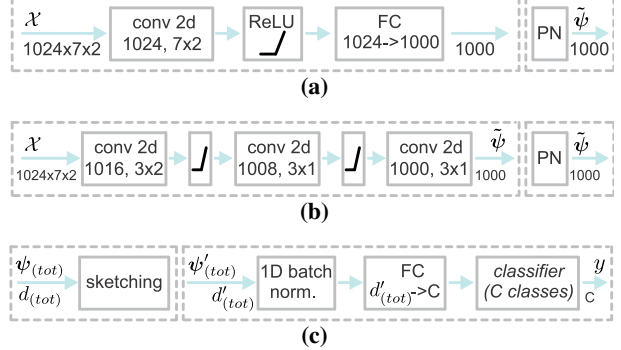


**Figure 2:** Stream types used in our network. Figures 2a and 2b show *Fully Connected* and *Convolutional* variants used for the practical realization of the FV, BoW, and HAF streams. Figure 2c shows our PredNet. Note that we indicate the type of operation and its parameters in each block e.g., *conv2d* and its number of filters/size, or *Power Normalization* (PN). Beneath arrows, we indicate the size of input, intermediate or output representation.

### 4.1. BoW/FV Hallucinating Streams

BoW/FV take as input the I3D intermediate representations  $\mathcal{X}_{(rgb)}$  and  $\mathcal{X}_{(opt.)}$  of size  $1024 \times 7$  which were obtained by stripping the classifier and the last 1D conv. layer of I3D pre-trained on Kinetics-400. The latter dimension of  $\mathcal{X}_{(rgb)}$  and  $\mathcal{X}_{(opt.)}$  can be thought of as the temporal size. We concatenate  $\mathcal{X}_{(rgb)}$  and  $\mathcal{X}_{(opt.)}$  along the third mode and obtain  $\mathcal{X}$  which has dimensionality  $1024 \times 7 \times 2$ . As FV contains the first- and second-order statistics, we use a separate stream per each type of statistics, and a single stream for BoW. For the practical choice of BoW/FV pipelines, we use either a Fully Connected (FC) unit shown in Figure 2a or a Convolutional (Conv) pipeline in Figure 2b. Thus, we investigate the following hallucinating stream combinations: (i) BoW-FC and FV-FC, or (ii) BoW-Conv and FV-Conv. Where indicated, we also equip each stream with Power Normalization (PN). For specific PN realizations, we investigate AsinhE, SigmE, and AxMin variants from Remarks 1, 2 and 3. Below we detail how we obtained ground-truth BoW/FV.

**Ground-truth BoW/FV.** To train Fisher Vectors, we computed 256 dimensional GMM-based dictionaries on descriptors resulting from IDT [60] according to steps described in Sections 2 and 3.1. We applied PCA to trajectories (30 dim.), HOG (96 dim.), HOF (108 dim.), MBHx (96 dim.) and MBHy (96 dim.), and we obtained the final 213 dim. local descriptors. We applied encoding as in Eq. (2) and (3), the aggregation from Section 3.2 and Power Normalization from Section 3.3. Thus, our encoded first- and second-order FV representations, each of size  $256 \times 213 = 54528$ , had to be sketched to 1000 dimensions. To this end, we followed Section 3.4, prepared matrices  $\mathbf{P}_{(fv1)}$  and  $\mathbf{P}_{(fv2)}$  as in Proposition 2, and fixed both of them throughout experiments. The sketched first- and second-order representations  $\psi'_{(fv1)} = \mathbf{P}_{(fv1)}\psi_{(fv1)}$  and

$\psi'_{(fv2)} = \mathbf{P}_{(fv2)} \psi_{(fv2)}$  can be readily combined next with the MSE loss functions detailed in Section 4.4.

For BoW, we followed Section 3.1 and applied k-means to build a 1000 dim. dictionary from the same descriptors which were employed to pre-compute FV. Then, the descriptors were encoded according to Eq. (1), aggregated according to steps described in Section 3.2 and normalized by Power Normalization from Section 3.3. Where indicated, we used 4000 dim. dictionary and thus applied sketching on such BoW to limit its vector size to 1000 dim.

We note that we use ground-truth BoW/FV descriptors only at the training stage to train our hallucination streams.

## 4.2. High Abstraction Features

High Abstraction Features (HAF) take as input the I3D intermediate representations  $\mathcal{X}_{(rgb)}$  and  $\mathcal{X}_{(opt.)}$ . Practical realizations of HAF pipelines are identical to those of BoW/FV. Thus, we have a choice of either FC or Conv units illustrated in Figures 2a and 2b. We simply refer to those variants as HAF-FC and HAF-Conv, respectively. Similar to BoW/FV streams, the HAF representation also uses Power Normalizing functions and it is of size 1000.

## 4.3. Combining Hallucinated BoW/FV with HAF

Figure 1 indicates that FV (first- and second-order), BoW and HAF feature vectors  $\tilde{\psi}_{(fv1)}$ ,  $\tilde{\psi}_{(fv2)}$ ,  $\tilde{\psi}_{(bow)}$  and  $\psi_{(haf)}$  are concatenated (via operator  $\oplus$ ) to obtain  $\psi_{(tot)}$  and subsequently sketched (if indicated so during experiments), that is,  $\psi'_{(tot)} = \mathbf{P}_{(tot)} \psi_{(tot)}$  which reduces the size of the total representation from  $d=4000$  to  $500 \leq d' \leq 2000$ . Matrix  $\mathbf{P}_{(tot)}$  is prepared according to Proposition 2 and fixed throughout experiments. As sketching is a linear projection, we can backpropagate through it with ease.

**PredNet.** The final unit of our overall pipeline, PredNet, is illustrated in Figure 2c. On input, we take  $\psi_{(tot)}$  (no sketching) or  $(\psi'_{(tot)})$  if sketching is used, pass it via the batch normalization and then an FC layer which produces a  $C$  dim. representation passed to the cross-entropy loss.

## 4.4. Objective and its Optimization

During training, we combine MSE loss functions responsible for training hallucination streams with the class. loss:

$$\ell^*(\mathbf{X}, \mathbf{y}; \Theta) = \frac{\alpha}{|\mathcal{H}|} \sum_{i \in \mathcal{H}} \|\tilde{\psi}_i - \psi'_i\|_2^2 + \ell\left(f(\psi'_{(tot)}; \Theta_{(pr)}), \mathbf{y}; \Theta_{(\ell)}\right),$$

where:  $\forall i \in \mathcal{H}, \tilde{\psi}_i = g(\tilde{\psi}_i; \Theta_i, \eta), \psi'_i = \mathbf{P}_i \psi_i, \psi_{(haf)} = g(\psi_{(haf)}; \Theta_{(haf)}, \eta), \psi'_{(tot)} = \mathbf{P}_{(tot)} \left[ \oplus_{i \in \mathcal{H}} \tilde{\psi}_i; \psi_{(haf)} \right]$ . (8)

The above equation is a trade-off between the MSE loss functions  $\{\|\tilde{\psi}_i - \psi'_i\|_2^2, i \in \mathcal{H}\}$  and the classification loss  $\ell(\cdot, \mathbf{y}; \Theta_{(\ell)})$  with some label  $\mathbf{y} \in \mathcal{Y}$  and parameters  $\Theta_{(\ell)} \equiv$

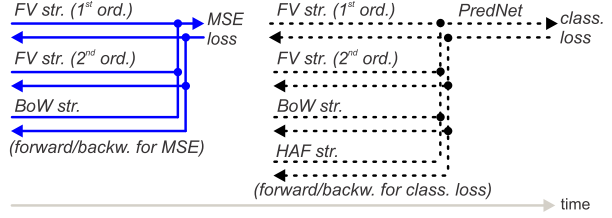


**Figure 3:** Our training procedure. In each step, we have (i) forward/backward passes via BoW/FV streams regarding the MSE loss followed by (ii) forward/backward passes via FV, BoW, HAF streams and PredNet regarding the classification loss.

$\{\mathbf{W}, \mathbf{b}\}$ . The trade-off is controlled by a constant  $\alpha \geq 0$  while MSE is computed over hallucination streams  $i \in \mathcal{H}$ , and  $\mathcal{H} \equiv \{(fv1), (fv2), (bow)\}$  is our set of hallucination streams which can be modified to multiple/few such streams depending on the task at hand. Moreover,  $g(\cdot, \eta)$  is a Power Normalizing function chosen from the family described in Section 3.3,  $f(\cdot; \Theta_{(pr)})$  is the PredNet module with parameters  $\Theta_{(pr)}$  which we learn,  $\{\tilde{\psi}_i, i \in \mathcal{H}\}$  are the hallucination streams while  $\{\tilde{\psi}_i, i \in \mathcal{H}\}$  are the corresponding hallucinated BoW/FV representations. Moreover,  $\tilde{\psi}_{(haf)}$  is the HAF stream with the output denoted by  $\psi_{(haf)}$ . For the hallucination streams, we learn parameters  $\{\Theta_i, i \in \mathcal{H}\}$  while for HAF, we learn  $\Theta_{(haf)}$ . The full set of parameters we learn is defined as  $\Theta \equiv \{(\Theta_i, i \in \mathcal{H}), \Theta_{(haf)}, \Theta_{(pr)}, \Theta_{(\ell)}\}$ . Furthermore,  $\{\mathbf{P}_i, i \in \mathcal{H}\}$  are the projection matrices for count sketching of the ground-truth BoW/FV feature vectors  $\{\psi_i, i \in \mathcal{H}\}$  while  $\{\psi'_i, i \in \mathcal{H}\}$  are the corresponding sketched/compressed representations. Finally,  $\mathbf{P}_{(tot)}$  is the projection matrix for hallucinated BoW/FV representations concatenated with each other and with HAF, that is, for  $\psi_{(tot)} = \left[ \oplus_{i \in \mathcal{H}} \tilde{\psi}_i; \psi_{(haf)} \right]$  which results in the sketched counterpart  $\psi'_{(tot)}$  that goes into the PredNet module  $f$ . Section 3.4 details how to select matrices  $\mathbf{P}$ . If sketching is not needed, we simply set a given  $\mathbf{P}$  to be the identity projection  $\mathbf{P} = \mathbb{I}$ . In our experiments, we simply set  $\alpha = 1$ .

**Optimization.** We minimize  $\ell^*(\mathbf{X}, \mathbf{y}; \bar{\Theta})$  w.r.t. parameters of each stream, that is  $\{\Theta_i, i \in \mathcal{H}\}$  for hallucination streams,  $\Theta_{(haf)}$  for the HAF stream,  $\Theta_{(pr)}$  for PredNet and  $\Theta_{(\ell)}$  for the classification loss. In practice, we perform a simple alternation over two minimization steps shown in Figure 3. In each iteration, we perform one forward and backward pass regarding the MSE losses to update the parameters  $\{\Theta_i, i \in \mathcal{H}\}$  of the hallucination streams. Then, we perform one forward and backward pass regarding the classification loss  $\ell$ . We update all network streams during this pass. Thus, one can think of our network as a multitask learning pipeline with BoW/FV and label learning tasks. Furthermore, we use the Adam minimizer with  $1e-4$  initial learning rate which we halve every 10 epochs. We run our training for 50–100 epochs depending on the dataset.

	<i>sp1</i>	<i>sp2</i>	<i>sp3</i>	mean acc.
HAF only	81.83%	80.78%	80.45%	81.02%
HAF+BoW/FV exact	83.00%	82.80%	81.70%	<b>82.50%</b>
HAF+BoW halluc.	82.29%	81.24%	80.98%	81.50%
HAF+FV halluc.	82.68%	81.05%	79.93%	81.22%
HAF+BoW/FV halluc.	82.88%	82.74%	81.50%	<b>82.37%</b>

**Table 1:** Evaluations of pipelines on the HMDB-51 dataset. We compare (*HAF only*) and (*HAF+BoW/FV exact*) which show the lower- and upper bound on the accuracy, and our (*HAF+BoW/FV halluc.*), (*HAF+BoW halluc.*) and (*HAF+FV halluc.*).

	<i>static</i>	<i>dynamic</i>	<i>mixed</i>	mean acc.
HAF only	92.03%	81.67%	89.07%	87.59%
HAF+BoW/FV exact	93.30%	89.82%	92.41%	91.84%
HAF+BoW halluc.	92.69%	85.93%	92.41%	90.34%
HAF+FV halluc.	92.69%	88.15%	91.48%	90.77%
HAF+BoW/FV halluc.	93.15%	89.63%	92.31%	<b>91.69%</b>

**Table 2:** Eval. of pipelines on YUP++. See Table 1 for the legend.

### Sketching the Power Normalized vectors.

**Proposition 3.** *Sketching PN vectors increases the sketching variance ( $\ell_2$ -normalized by vec. norms) by  $1 \leq \kappa \leq 2$ .*

*Proof.* Normalize variance  $\mathbb{V}$  from Remark 4 by the norms  $\|\psi\|_2^2 \|\psi'\|_2^2$ . Consider  $\mathbb{V}^{(\gamma)}$  which is the variance for  $d$  dimensional vectors  $\{(\psi^\gamma, \psi'^\gamma) : \psi \geq 0, \psi' \geq 0\}$  power normalized by Gamma from Remark 1, and divide it accordingly by  $\|\psi^\gamma\|_2^2 \|\psi'^\gamma\|_2^2$ . For extreme PN ( $\gamma \rightarrow 0$ ), we have:

$$\lim_{\gamma \rightarrow 0} \mathbb{V}^{(\gamma)} = \frac{1}{d'} \lim_{\gamma \rightarrow 0} \left( \frac{\langle \psi^\gamma, \psi'^\gamma \rangle^2}{\|\psi^\gamma\|_2^2 \|\psi'^\gamma\|_2^2} + 1 \right) = \frac{2}{d'}. \quad (9)$$

Now, assume that  $d$  dimensional  $\psi$  and  $\psi'$  are actually  $\ell_2$ -norm normalized. Then, we have the following ratio of variances:

$$\kappa = \mathbb{V} / \mathbb{V}^{(\gamma)} = 2 / (\langle \psi, \psi' \rangle^2 + 1), \quad (10)$$

Thus,  $1 \leq \kappa \leq 2$  depends on  $(\psi, \psi')$ , and  $\kappa$  varies smoothly between  $[1; 2]$  for  $1 \leq \gamma \leq 0$  of Gamma, a monotonically increasing function. For typical  $\gamma = 0.5$ , we measured for the actual data that  $\kappa \approx 1.3$ .  $\square$

## 5. Experiments

Below we describe datasets/protocols, and we validate usefulness of our pipeline. We do not stake claims that we beat every single AR pipeline nor this is our goal. As the majority of AR pipelines use IDT descriptors to boost their performance [27, 4, 7, 8, 61], in this paper, we simply show how to put new life into handcrafted IDT descriptors by learning and then synthesizing them by a CNN pipeline.

### 5.1. Datasets and Evaluation Protocols

**HMDB-51** [38] consists of 6766 internet videos over 51 classes; each video has  $\sim 20$ –1000 frames. Following the protocol, we report the mean accuracy across three splits.

**YUP++** [17] dataset contains so-called video textures. It has 20 scene classes, 60 videos per class, and its splits contain scenes captured with the static or moving camera. We follow the standard splits (1/9 dataset for training).

**MPII Cooking Activities** [48] consist of high-resolution videos of people cooking various dishes. The 64 distinct activities from 3748 clips include coarse actions *e.g.*, *opening refrigerator*, and fine-grained actions *e.g.*, *peel*, *slice*, *cut apart*. We use the mean Average Precision (mAP) over 7-fold crossvalidation. For human-centric protocol [6, 8], we use Faster-RCNN [46] to crop video around humans.

### 5.2. Evaluations

We start our experiments by investigating various aspects of our pipeline and then we present our final results.

**HAF, BoW and FV streams.** Firstly, we ascertain the gains from our HAF and BoW/FV streams. We evaluate the performance of (i) the HAF-only baseline pipeline without IDT-based BoW/FV information (*HAF only*), (ii) the HAF-only baseline with exact ground-truth IDT-based BoW/FV added at both training and testing time (*HAF+BoW/FV exact*), and (iii) the combined HAF plus IDT-based BoW/FV streams (*HAF+BoW/FV halluc.*). We also perform evaluations on (iv) HAF plus IDT-based BoW stream (*HAF+BoW halluc.*) and HAF plus IDT-based FV stream (*HAF+FV halluc.*) to examine how much gain IDT-based BoW and FV bring, respectively. As Section 4.1 suggests that each stream can be based on either the Fully Connected (FC) or Convolutional (Conv.) pipeline, we firstly investigate the use of FC unit from Figure 2a, that is, we use HAF-FC, BoW-FC and HAF-FC streams. PredNet also uses FC. For ground-truth FV, we use 1000 dim. sketches.

Table 1 presents results on the HMDB-51 dataset. As expected, the (*HAF only*) is the poorest performer while (*HAF+BoW/FV exact*) is the best performer determining the upper limit on the accuracy. Hallucinating (*HAF+BoW halluc.*) outperforms (*HAF+FV halluc.*) marginally. We expect FV to perform close to BoW due to the significant compression with sketching by factor 52.5 $\times$ . Approaches (*HAF+FV/BoW halluc.*) and (*HAF+BoW/FV exact*) achieve the best results, and outperform (*HAF only*) by 1.35% and 1.48% accuracy. These result show that our hallucination strategy (*HAF+FV/BoW halluc.*) can mimic (*HAF+BoW/FV exact*) closely. Our 82.37% accuracy is the new state of the art. Below we show larger gains on YUP++.

Table 2 presents similar findings on the YUP++ dataset. Our (*HAF+FV halluc.*) brings the improvement of 2.2 and 6.5% over (*HAF+BoW halluc.*) and (*HAF only*) on scenes captured with the moving camera (*dynamic*). Our (*HAF+BoW/FV halluc.*) yields 8.0% over (*HAF only*) thus demonstrating again the benefit of hallucinating BoW/FV descriptors. The total gain for (*HAF+BoW/FV halluc.*) over (*HAF only*) equals 4.1%. Note that our (*HAF+FV/BoW*

	<i>sp1</i>	<i>sp2</i>	<i>sp3</i>	mean acc.
HAF-Conv+BoW/FV-FC halluc.	81.96%	80.39%	80.52%	80.95%
HAF-FC+BoW/FV-Conv halluc.	82.42%	81.30%	81.50%	81.74%
HAF-FC+BoW/FV-FC halluc.	82.88%	82.74%	81.50%	<b>82.37%</b>

**Table 3:** Evaluations of pipelines on the HMDB-51 dataset. We compare (*HAF+BoW/FV halluc.*) approach on different architectures used for HAF and BoW/FV streams such as (*FC*) and (*Conv*).

*halluc.*) matches results of (*HAF+BoW/FV exact*) without explicitly computing BoW/FV during testing. Below, we briefly investigate different architectures for our streams.

**Fully Connected/Convolutional streams.** Figures 2a and 2b show two possible realizations of HAF, BoW and FV streams. While FC and Conv. architectures are not the only possibilities, they are the simplest ones. Table 3 shows that using FC layers (*FC*) for HAF and BoW/FV streams, denoted as (*HAF-FC+BoW/FV-FC halluc.*) outperforms Convolutional (*Conv*) variants by up to  $\sim 1.5\%$  accuracy. Thus, we use only the FC architecture in what follows.

**Sketching and Power Normalization.** Below, we investigate the impact of Power Normalization and count sketching presented in Sections 3.3 and 3.4 on the accuracy. As PredNet uses FC layers, as shown in Figure 2c, we expect that limiting the input size to this layer should benefit the performance. Moreover, as visual and video representations are known to suffer from so-called burstiness, we investigate AsinhE, SigmE and AxMin from Remarks 1, 2 and 3.

Figure 4a investigates the classification accuracy on the HMDB-51 dataset (split 1) when our HAF and BoW/FV feature vectors  $\{\psi_i, i \in \mathcal{H}\}$  and  $\psi_{(haf)}$  (described in Sections 4.3 and 4.4) are passed via Power Normalizing functions AsinhE, SigmE and AxMin prior to concatenation (see Figure 1 for reference). From our experiment it appears that all PN functions perform similarly and improve results from the baseline 82.29% to  $\sim 83.20\%$  accuracy. In what follows, we simply use AsinhE for PN. Similar trend is observed on the YUP++ dataset *e.g.*, for the split (*static*), we observed an improvement from 93.15 to 94.44% accuracy.

Figure 4b illustrates on the HMDB-51 dataset (split 1) that applying count sketching on concatenated HAF and BoW/FV feature vectors  $\psi_{(tot)}$ , which produces  $\psi'_{(tot)}$  (see Section 4.4 for reference to symbols), improves results from 82.88 to 83.92% accuracy for  $d' = 2000$ . This is expected

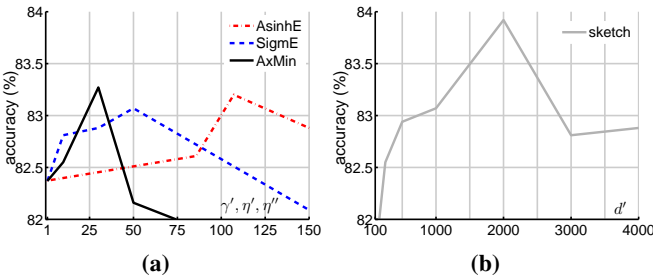


**Figure 4:** Evaluations of (fig. 4a) Power Normalization and (fig. 4b) sketching on the HMDB-51 dataset (split 1 only).

	<i>sp1</i>	<i>sp2</i>	<i>sp3</i>	mean acc.
HAF only	81.83%	80.78%	80.45%	81.02%
HAF+BoW/FV halluc.	83.46%	82.61%	81.37%	<b>82.48%</b>
ADL+ResNet+IDT [62]	74.3%	STM Network+IDT [16]	72.2%	
ADL+I3D [62]	81.5%	Full-FT I3D [4]	81.3%	

**Table 4:** Evaluations of (*top*) our (*HAF+BoW/FV halluc.*) and (*bottom*) comparisons to the state of the art on HMDB-51.

	<i>static</i>	<i>dynamic</i>	<i>mixed</i>	mean stat/dyn	mean all
HAF only	92.03%	81.67%	89.07%	86.8%	87.6%
HAF+BoW/FV halluc.	94.81%	<b>89.63%</b>	<b>93.33%</b>	<b>92.2%</b>	<b>92.6%</b>
T-ResNet [17]	92.41%	81.50%	89.00%	87.0%	87.6%
ADL I3D [62]	<b>95.10%</b>	88.30%	-	91.7%	-

**Table 5:** Evaluations of (*top*) our (*HAF+BoW/FV halluc.*) and (*bottom*) comparisons to the state of the art on YUP++.

	<i>sp1</i>	<i>sp2</i>	<i>sp3</i>	<i>sp4</i>	<i>sp5</i>	<i>sp6</i>	<i>sp7</i>	mAP
HAF+BoW halluc.	73.9	71.6	76.2	70.7	76.32	71.9	63.4	71.9%
HAF+BoW halluc.+SK/PN	73.9	75.8	72.2	73.9	77.0	73.6	68.8	<b>73.6%</b>
HAF* only	74.6	73.2	77.0	75.1	76.1	75.6	71.9	74.8%
HAF*+BoW halluc.	78.8	75.0	84.1	76.0	77.0	78.3	75.2	<b>77.8%</b>
HAF*+BoW hal.+MSK/PN	80.1	79.2	84.8	83.9	80.9	78.5	75.5	<b>80.4%</b>
KRP-FS 70.0% [8]	KRP-FS+IDT 76.1% [8]	GRP 68.4% [6]	GRP+IDT 75.5% [6]					

**Table 6:** Evaluations of (*top*) our (*HAF+BoW halluc.*) pipeline without sketching/PN, with sketching/PN (*SK/PN*). The (*HAF\* only*) is our baseline without the BoW stream, (\*) denotes human-centric pre-processing while (*MSK/PN*) in pipeline (*HAF\*+BoW hal.+MSK/PN*) denotes multiple sketches per BoW followed by Power Norm (*PN*). (*bottom*) Other methods on the MPII dataset.

as reduced size of  $\psi'_{(tot)}$  results in fewer parameters of the FC layer of PredNet and less overfitting. Similarly, for the YUP++ dataset and the split (*static*), we see the performance increase from 93.15 to 94.44% accuracy.

**Comparisons with other methods.** Below we present our final results and we contrast them against the state of the art. Table 4 shows results on the HMDB-51 dataset. For our method, we used sketching of  $\psi_{(tot)}$  with  $d' = 2000$  and PN. Our (*HAF+BoW/FV halluc.*) model yields 82.48% acc. which beats results in the literature to the best of our knowledge. If we tune PN per split, our results reach 82.78% accuracy. However, we do not advise such tuning due to danger of overfitting. We note that we outperform more complex methods such as Adversarial Discriminative Learning (ADL) with I3D [62] and Fully Fine-Tuned I3D [4].

Table 5 shows results on the YUP++ dataset. Our (*HAF+BoW/FV halluc.*) model yields very competitive results on the static protocol and outperforms competitors on the dynamic and mixed protocols. With 92.2% mean accuracy over static and dynamic scores (*mean stat/dyn*), we outperform more complex ADL+I3D [62] and T-ResNet [17].

Table 6 shows results for the MPII dataset for which we use HAF with/without the BoW (4000 dim.) hallucination stream (no FV stream). As MPII contains subse-

quences, we use integral pooling from Prop. 1. Our basic model (*HAF+BoW halluc.*) scores  $\sim 71.9\%$  mAP. Applying sketching and PN (*HAF+BoW halluc.+SK/PN*) yields  $73.6\%$  mAP. Unlike GRP+IDT [6] and KRP-FS+IDT [8], our first two experiments do not use any human- or motion-centric pre-processing. With human-centric crops, denoted with (\*), our baseline without BoW (*HAF\* only*) achieves  $74.8\%$  mAP. The model with BoW (*HAF+BoW halluc.*) scores  $77.8\%$  mAP. By utilizing 4 sketches for BoW and 4 BoW streams with Power Normalization (*HAF\*+BoW hal.+MSK/PN*), we obtain  $80.4\%$  mAP, the new state of the art. This shows that despite a slight increase in sketching variance due to PN preceding sketching, as explained in Prop. 3, preventing overfitting/burritess in AR is vital.

## 6. Conclusions

We have proposed a simple yet powerful strategy which can absorb old-fashioned IDT descriptors and hallucinate them in CNN-based AR pipelines at the test time for the best accuracy. With state-of-the-art results, we hope our method will spark a renewed interest in IDT-like descriptors. Kindly see our supplementary material for further analysis/results.

# Appendices

Below we asses (i) the hallucination quality, (ii) provide additional results for higher resolution frames on MPII, and (iii) we provide further details of our pre-processing not detailed in the main submission.

## A. Hallucination Quality

Below, we provide an analysis of the quality of hallucination of the BoW/FV streams compared to the ground-truth BoW/FV feature vectors. Figure 5 presents histograms of the square difference between the hallucinated features and ground-truth ones. Specifically, we plot histograms of  $\{(\tilde{\psi}_{(bow),mn} - \psi_{(bow),mn})^2, m \in \mathcal{I}_{1000}, n \in \mathcal{N}\}$ , where index  $m$  runs over features  $m \in \mathcal{I}_{1000}$  and  $n \in \mathcal{N}$  runs over each video. Counts for training and testing splits are normalized by 1000 (the number of features) and the number of training and testing videos, respectively. The histograms are computed over bins of size 0.01 thus allowing us to simply plot continuously looking lines instead of bins.

Figure 5a shows that the BoW ground-truth descriptors for the training split are learnt closely by our BoW hallucinating unit based on FC layers (FC). We capture histograms for epochs 1, 5, 15, 25 in colors interpolated from red to blue. As one can see, in early epochs, the peak around the first bin is small. As the epochs progress, the peak around the first bin becomes prominent while further bins decrease

in size. This indicates that as the training epochs progress, the approximation error becomes smaller and smaller.

Figure 5b shows that the BoW ground-truth descriptors for the testing split are also approximated closely by the hallucinated BoW descriptors.

We compared histograms for testing and training slits for BoW, first- and second-order FV and observed small differences only. Such a comparison can be conducted by computing the ratio of testing to training bins and it reveals variations between  $0.8\times$  and  $1.25\times$ . Thus, without the loss of clarity, we skip showing plots for FV testing splits.

Figures 5c and 5d show that the first- and second-order FV terms (*FV1*) and (*FV2*) can be also learnt closely by our hallucinating units. We show only the quality of approximation on the training split as behavior on testing splits matches closely the behavior on training splits.

Figures 5e, 5f, 5g and 5h show the similar learning/approximation trend for BoW training and testing splits, and the first- and second-order FV terms (training only) given our hallucinating unit based on Convolutional layers (*Conv*). However, it appears that (*Conv*) learns slower to hallucinate FV descriptors if compared to BoW descriptors. We expect that our (*Conv*) unit has not enough learning capacity to fully approximate these representations.

## B. Higher Resolution Frames on MPII

For human-centric pre-processing on MPII denoted by (\*) in the main submission, we observed that the bounding boxes used for extraction of the human subject are of low resolution. Thus, we decided to firstly resize RGB frames to 512 pixels (height) rather than 256 pixels (as in our main submission) and then compute the corresponding optical flow, and perform extraction of human subjects for which the resolution thus increased  $2\times$ .

The (*HAF\*+BoW halluc.*), our pipeline with the BoW stream, and (*HAF\*+BoW hal.+MSK/PN*) with multiple sketches and PN are computed for the standard 256 pixels (height) denoted by (\*) are given in Table 7. Note that results for (\*) are taken from our main submission.

The (*HAF\*+BoW halluc.*), our pipeline with the BoW stream, and (*HAF\*+BoW hal.+MSK/PN*) pipeline are analogous pipelines but computed for the increased 512 pixel resolution (height) denoted by (\*). According to the table, increasing the resolution  $2\times$  prior to human detection, extracting subjects in higher resolution and scaling (to the 256 size for shorter side) yields 1.3% improvement in accuracy.

## C. Data Pre-processing

For HMDB-51 and YUP++, we use the data augmentation strategy described in the original authors' papers (e.g., random crop of videos, left-right flips on RGB and optical flow frames. For testing, center crop, no flipping are used.

	<i>sp1</i>	<i>sp2</i>	<i>sp3</i>	<i>sp4</i>	<i>sp5</i>	<i>sp6</i>	<i>sp7</i>	mAP
HAF*+BoW halluc.	78.8	75.0	84.1	76.0	77.0	78.3	75.2	77.8%
HAF*+BoW hal.+MSK/PN	80.1	79.2	84.8	83.9	80.9	78.5	75.5	80.4%
HAF•+BoW halluc.	78.8	78.3	84.2	77.4	77.1	78.3	75.2	78.5%
HAF•+BoW hal.+MSK/PN	80.8	80.9	85.0	83.9	82.0	79.8	79.6	<b>81.7%</b>

**Table 7:** Evaluations on MPII. The (*HAF\*+BoW halluc.*) is our pipeline with the BoW stream, (\*) denotes human-centric pre-processing for 256 pixels (height) while (*HAF\*+BoW hal.+MSK/PN*) denotes our pipeline with multiple sketches per BoW followed by Power Norm (*PN*). By analogy, (•) denotes human-centric pre-processing for 512 pixels (height).

For the MPII dataset with human-centric pre-processing, human detector is used first. Then, we crop randomly around the bounding box of human subject (we include it). Finally, we allow scaling, zooming in, and left-right flips. For longer videos, we sample sequences to form a 64-frame sequence. For short videos (less than 64 frames), we loop the sequence many times to fit its length to the expected input length. Lastly, we scale the pixel values of RGB and optical flow frames to the range between  $-1$  and  $1$ .

## References

- [1] L. Alvarez, J. Weickert, and J. Sánchez. Reliable estimation of dense optical flow fields with large displacements. *IJCV*, 39(1):41–56, Aug. 2000. 3
- [2] J. Braux-Zin, R. Dupont, and A. Bartoli. A general dense image matching framework combining direct and feature-based costs. In *ICCV*, pages 185–192, 2013. 3
- [3] T. Brox and J. Malik. Large displacement optical flow: Descriptor matching in variational motion estimation. *TPAMI*,
- [4] J. Carreira and A. Zisserman. Quo Vadis, Action Recognition? A New Model and the Kinetics Dataset. *CVPR*, pages 1–10, 2018. 1, 3, 7, 8
- [5] B. Chakraborty, M. B. Holte, T. B. Moeslund, and J. González. Selective spatio-temporal interest points. *CVIU*, 116(3):396–410, 2012. 2
- [6] A. Cherian, B. Fernando, M. Harandi, and S. Gould. Generalized rank pooling for action recognition. In *CVPR*, 2017. 7, 8, 9
- [7] A. Cherian, P. Koniusz, and S. Gould. Higher-order pooling of CNN features via kernel linearization for action recognition. In *WACV*, pages 130–138, 2017. 1, 2, 3, 7
- [8] A. Cherian, S. Sra, S. Gould, and R. Hartley. Non-linear temporal subspace representations for activity recognition. In *CVPR*, pages 2197–2206, 2018. 1, 2, 3, 7, 8, 9
- [9] V. Choutas, P. Weinzaepfel, J. Revaud, and C. Schmid. Potion: Pose motion representation for action recognition. In *CVPR*, pages 7024–7033, 2018. 1, 2, 3
- [10] G. Cormode and M. Hadjieleftheriou. Finding frequent items in data streams. *Proc. VLDB Endow.*, 1(2):1530–1541, Aug. 2008. 5
- [11] G. Csurka, C. R. Dance, L. Fan, J. Willamowski, and C. Bray. Visual categorization with bags of keypoints. *ECCV Workshop*, pages 1–22, 2004. 1, 3, 4
- [12] N. Dalal, B. Triggs, and C. Schmid. Human Detection Using Oriented Histogram of Flow and Appearance. *ECCV*, pages 428–441, 2006. 1, 2
- [13] P. Dollar, V. Rabaud, G. Cottrell, and S. Belongie. Behavior recognition via sparse spatio-temporal features. In *Proceedings of the 14th International Conference on Computer Communications and Networks*, ICCCN ’05, pages 65–72, 2005. 2
- [14] J. Donahue, L. A. Hendricks, S. Guadarrama, M. Rohrbach,

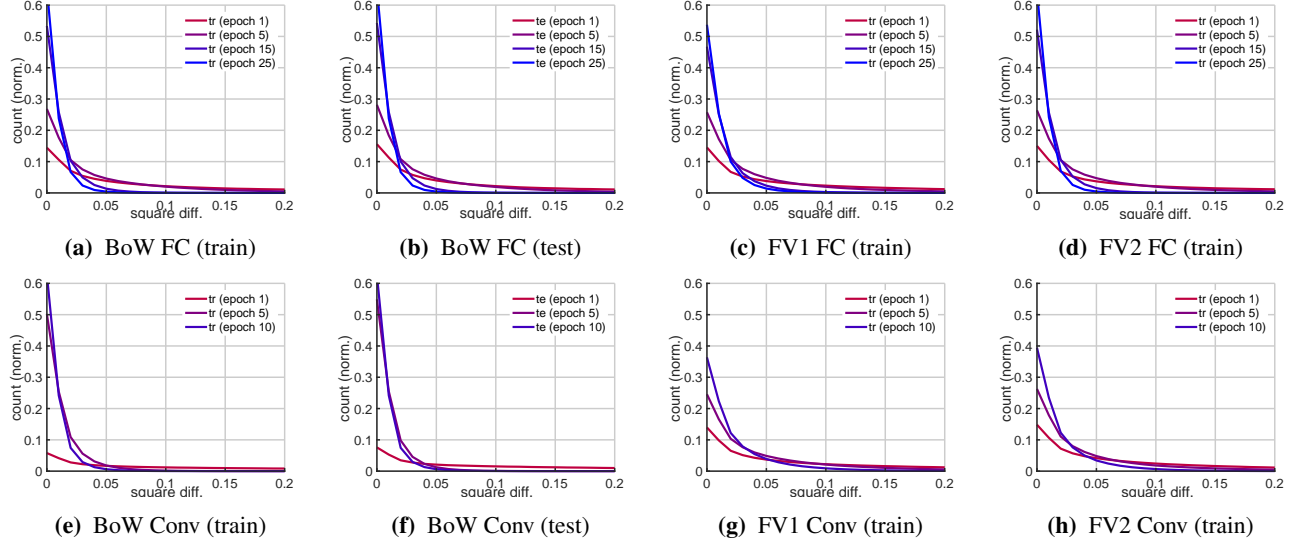


**Figure 5:** Evaluation of the square difference between the hallucinated and ground truth representations on HMDB-51 (split 1). Experiments in the top row use (*FC*) streams with sketching and *PN*. Experiments in the bottom row use (*Conv*) streams.

S. Venugopalan, T. Darrell, and K. Saenko. Long-term recurrent convolutional networks for visual recognition and description. In *CVPR*, pages 2625–2634, 2015. 3

[15] C. Feichtenhofer, A. Pinz, and R. P. Wildes. Spatiotemporal residual networks for video action recognition. In *NIPS*, pages 3468–3476, 2016. 1, 3

[16] C. Feichtenhofer, A. Pinz, and R. P. Wildes. Spatiotemporal multiplier networks for video action recognition. In *CVPR*, 2017. 8

[17] C. Feichtenhofer, A. Pinz, and R. P. Wildes. Temporal residual networks for dynamic scene recognition. In *CVPR*, 2017. 7, 8

[18] B. Fernando, E. Gavves, J. O. M., A. Ghodrati, and T. Tuytelaars. Modeling video evolution for action recognition. In *CVPR*, pages 5378–5387, 2015. 3

[19] B. Fernando and S. Gould. Learning end-to-end video classification with rank-pooling. In *ICML*, volume 48, pages 1187–1196, 2016. 1, 2, 3

[20] W. T. Freeman and M. Roth. Orientation histograms for hand gesture recognition. Technical Report TR94-03, MERL - Mitsubishi Electric Research Laboratories, Cambridge, MA 02139, Dec. 1994. 1, 2

[21] S. Gauglitz, T. Höllerer, and M. Turk. Evaluation of interest point detectors and feature descriptors for visual tracking. *IJCV*, 94(3):335, Mar 2011. 2

[22] M. Harandi, M. Salzmann, and R. Hartley. Dimensionality reduction on spd manifolds: The emergence of geometry-aware methods. *TPAMI*, 2018. 4

[23] S. Herath, M. Harandi, B. Fernando, and R. Nock. Min-max statistical alignment for transfer learning. *CVPR*, 2019. 4

[24] B. K. P. Horn and B. G. Schunck. Determining optical flow. *Artificial Intelligence*, 17:185–203, 1981. 3

[25] I. M. L. Hunter. Book review: Thinking in perspective: Critical essays in the study of thought processes. *Quarterly Journal of Experimental Psychology*, 32(2):358–359, 1980. 3

[26] H. Jégou, M. Douze, and C. Schmid. On the Burstiness of Visual Elements. *CVPR*, pages 1169–1176, 2009. 3

[27] S. Ji, W. Xu, M. Yang, and K. Yu. 3d convolutional neural networks for human action recognition. *TPAMI*, 35:221–231, 2010. 3, 7

[28] A. Karpathy, G. Toderici, S. Shetty, T. Leung, R. Sukthankar, and L. Fei-Fei. Large-scale video classification with convolutional neural networks. In *CVPR*, CVPR '14, pages 1725–1732, 2014. 3

[29] A. Klaser, M. Marszalek, and C. Schmid. A Spatio-Temporal Descriptor Based on 3D-Gradients. *BMCV*, pages 1–10, 2008. 1, 2

[30] P. Koniusz, A. Cherian, and F. Porikli. Tensor representations via kernel linearization for action recognition from 3D skeletons. *ECCV*, 2016. 3

[31] P. Koniusz and K. Mikolajczyk. Soft Assignment of Visual Words as Linear Coordinate Coding and Optimisation of its Reconstruction Error. *ICIP*, 2011. 3

[32] P. Koniusz, Y. Tas, and F. Porikli. Domain adaptation by mixture of alignments of second- or higher-order scatter tensors. *CVPR*, 2, 2017. 4

[33] P. Koniusz, F. Yan, P. Gosselin, and K. Mikolajczyk. Higher-order Occurrence Pooling on Mid- and Low-level Features: Visual Concept Detection. *Technical Report*, 2013. 3

[34] P. Koniusz, F. Yan, P.-H. Gosselin, and K. Mikolajczyk. Higher-order occurrence pooling for bags-of-words: Visual concept detection. *TPAMI*, 39(2):313–326, 2017. 2, 3, 4

[35] P. Koniusz, F. Yan, and K. Mikolajczyk. Comparison of Mid-Level Feature Coding Approaches And Pooling Strategies in Visual Concept Detection. *CVIU*, 2012. 2, 3, 4

[36] P. Koniusz, H. Zhang, and F. Porikli. A deeper look at power normalizations. In *CVPR*, pages 5774–5783, 2018. 2, 3, 4

[37] A. Krizhevsky, I. Sutskever, and G. E. Hinton. ImageNet classification with deep convolutional neural networks. *NIPS*, pages 1106–1114, 2012. 3

[38] H. Kuehne, H. Jhuang, E. Garrote, T. Poggio, and T. Serre. Hmdb: a large video database for human motion recognition. In *ICCV*, pages 2556–2563. IEEE, 2011. 7

[39] I. Laptev. On space-time interest points. *IJCV*, 64(2-3):107–123, Sept. 2005. 2

[40] C. Li, B. Su, J. Wang, and Q. Zhang. Human action recognition using multi-velocity steps and motion energy orientation histogram. *J. Inf. Sci. Engg.*, 30:295–312, 2014. 2

[41] L. Lingqiao, L. Wang, and X. Liu. In Defence of Soft-assignment Coding. *ICCV*, 2011. 3

[42] N. Papenberg, A. Bruhn, T. Brox, S. Didas, and J. Weickert. Highly accurate optic flow computation with theoretically justified warping. *IJCV*, 67:141–158, 2006. 3

[43] F. Perronnin and C. Dance. Fisher kernels on visual vocabularies for image categorization. *CVPR*, 0:1–8, 2007. 1, 3, 4

[44] F. Perronnin, J. Sánchez, and T. Mensink. Improving the Fisher Kernel for Large-Scale Image Classification. *ECCV*, pages 143–156, 2010. 1, 3, 4

[45] N. Pham and R. Pagh. Fast and scalable polynomial kernels via explicit feature maps. In *Proceedings of the 19th ACM SIGKDD International Conference on Knowledge Discovery and Data Mining*, KDD '13, pages 239–247. ACM, 2013. 2, 5

[46] S. Ren, K. He, R. Girshick, and J. Sun. Faster r-cnn: Towards real-time object detection with region proposal networks. In *NIPS*, pages 91–99, 2015. 7

[47] J. Revaud, P. Weinzaepfel, Z. Harchaoui, and C. Schmid. EpicFlow: Edge-Preserving Interpolation of Correspondences for Optical Flow. In *CVPR*, 2015. 3

[48] M. Rohrbach, S. Amin, M. Andriluka, and B. Schiele. A database for fine grained activity detection of cooking activities. In *CVPR*, 2012. 7

[49] O. Russakovsky, J. Deng, H. Su, J. Krause, S. Satheesh, S. Ma, Z. Huang, A. Karpathy, A. Khosla, M. Bernstein, A. C. Berg, and L. Fei-Fei. ImageNet large scale visual recognition challenge. *IJCV*, 115(3):211–252, 2015. 3

[50] P. Scovanner, S. Ali, and M. Shah. A 3-Dimensional SIFT Descriptor and its Application to Action Recognition. *CRCV*, pages 1–4, 2007. 1, 2, 3

[51] K. Simonyan and A. Zisserman. Two-stream convolutional networks for action recognition in videos. In *NIPS*, pages 568–576, 2014. 1, 3

[52] J. Sivic and A. Zisserman. Video Google: A text retrieval approach to object matching in videos. *ICCV*, 2:1470–1477, 2003. 1, 3, 4

[53] Y. Tas and P. Koniusz. Cnn-based action recognition and supervised domain adaptation on 3d body skeletons via kernel feature maps. *BMVC*, 2018. 4

[54] D. Tran, L. Bourdev, R. Fergus, L. Torresani, and M. Paluri.

Learning Spatiotemporal Features with 3D Convolutional Networks. *ICCV*, pages 4489–4497, 2015. 1, 3

[55] J. Uijlings, I. Duta, N. Rostamzadeh, and N. Sebe. Realtime Video Classification using Dense HOF/HOG. *ICMR*, 2014. 2

[56] J. C. van Gemert, C. J. Veenman, A. W. M. Smeulders, and J.-M. Geusebroek. Visual word ambiguity. *TPAMI*, 32(7):1271–1283, July 2010. 3

[57] G. Varol, I. Laptev, and C. Schmid. Long-term temporal convolutions for action recognition. *TPAMI*, 40(6):1510–1517, 2018. 3

[58] H. Wang, A. Klaser, C. Schmid, and L. Cheng-Lin. Action Recognition by Dense Trajectories. *CVPR*, pages 3169–3176, 2011. 1, 2, 3

[59] H. Wang, A. Klaser, C. Schmid, and C.-L. Liu. Dense Trajectories and Motion Boundary Descriptors for Action Recognition. *IJCV*, 2013. 1, 2, 3

[60] H. Wang and C. Schmid. Action Recognition with Improved Trajectories. *ICCV*, pages 3551–3558, 2013. 1, 2, 5

[61] J. Wang and A. Cherian. Learning discriminative video representations using adversarial perturbations. In *ECCV*, pages 716–733, 2018. 1, 2, 3, 7

[62] J. Wang and A. Cherian. Learning discriminative video representations using adversarial perturbations. In *ECCV*, 2018. 8

[63] K. Weinberger, A. Dasgupta, J. Langford, A. Smola, and J. Attenberg. Feature hashing for large scale multitask learning. In *ICML*, pages 1113–1120, 2009. 4, 5

[64] P. Weinzaepfel, J. Revaud, Z. Harchaoui, and C. Schmid. DeepFlow: Large displacement optical flow with deep matching. In *ICCV*, 2013. 3

[65] G. Willems, T. Tuytelaars, and L. Gool. An efficient dense and scale-invariant spatio-temporal interest point detector. In *ECCV*, *ECCV '08*, pages 650–663, 2008. 2, 3

[66] L. Yeffet and L. Wolf. Local trinary patterns for human action recognition. *ICCV*, pages 492–497, 2009. 3